



Research papers

Infiltration on sloping terrain and its role on runoff generation and slope stability

Hugo A. Loáiciga*, J. Michael Johnson

Department of Geography, University of California, Santa Barbara, CA 93106, USA

ARTICLE INFO

Keywords:

Infiltration
Kinematic wave
Runoff
Factor of safety
Landslides
Rainfall

ABSTRACT

A modified Green-and-Ampt model is formulated to quantify infiltration on sloping terrain underlain by homogeneous soil wetted by surficial water application. This paper's theory for quantifying infiltration relies on the mathematical statement of the coupled partial differential equations (pdes) governing infiltration and runoff. These pdes are solved by employing an explicit finite-difference numerical method that yields the infiltration, the infiltration rate, the depth to the wetting front, the rate of runoff, and the depth of runoff everywhere on the slope during external wetting. Data inputs consist of a water application rate or the rainfall hyetograph of a storm of arbitrary duration, soil hydraulic characteristics and antecedent moisture, and the slope's hydraulic and geometric characteristics. The presented theory predicts the effect an advancing wetting front has on slope stability with respect to translational sliding. This paper's theory also develops the 1D pde governing suspended sediment transport and slope degradation caused by runoff influenced by infiltration. Three examples illustrate the application of the developed theory to calculate infiltration and runoff on a slope and their role on the stability of cohesive and cohesionless soils forming sloping terrain.

1. Introduction

This paper develops and tests a numerical model for the prediction of infiltration, runoff, and soil stability in slopes subjected to water application by rainfall or other forms of surficial water application (e.g., irrigation). Our work also develops the 1D pde governing suspended sediment transport and slope degradation caused by runoff influenced by infiltration. Fig. 1 depicts the geometry considered in this work, showing a slope with angle θ , length L , and width b perpendicular to the plane of the figure. A water application rate or rainfall rate $r(t)$ wets the slope. The rate of water application could be caused by artificial means, such as irrigation. The water application rate may cause runoff on the slope if it exceeds the infiltration rate g . In that case the variable depth of runoff is denoted by d in Fig. 1. The water pressure exerted by a water depth d equals $d \cdot \cos\theta \cdot \gamma_w$, as shown in Fig. 1, with γ_w denoting the unit weight of water ($= 9.81 \text{ kN/m}^3$).

The equations governing runoff and infiltration on sloping terrain are derived relying on Cartesian coordinates s and z shown in Fig. 1. The axis of the s coordinate is parallel to the slope surface and s increases downslope. The axis of the coordinate z is normal to the axis s and increases downwards from the slope surface. The runoff on the slope varies with distance s and with time, and is denoted by $q(s, t)$. It is seen in Fig. 1 that the infiltration rate has components equal to $g \cos \theta$

and $g \sin \theta$ along the coordinates z and s , respectively. The slope's soil has a volumetric water-content deficit equal to $w_o = n - v_o$ prior to the onset of infiltration, in which n denotes the porosity of the soil and v_o represents the antecedent volumetric water content. The depth to the wetting front varies along the slope and is represented by two variables, z_{vf} and z_f . The former variable is measured vertically downward from the slope surface, and the latter is measured downward from the slope surface along the coordinate axis z as depicted in Fig. 1. The infiltration, is denoted by G (units of length), whose time derivative equals the infiltration rate (i.e., $\partial G / \partial t = g$) (units of length over time). The volume of water entering the soil fills the available pore space ($n - v_o$) as it moves vertically downward. On a per unit area of slope such volume of water equals the infiltration G , which, in turn, equals the depth of water penetration times the available pore space that fills with entering water. This reasoning, in conjunction with the geometry of the coordinates aligned with the vertical axis and with the axis normal to the slope surface, leads to Eqs. (1) and (2) expressing respectively the depths z_{vf} and z_f in terms of the infiltration and the volumetric water-content deficit as follows:

$$z_{vf} = \frac{G}{n - v_o} \quad (1)$$

* Corresponding author.

E-mail address: hloaiciga@ucsb.edu (H.A. Loáiciga).

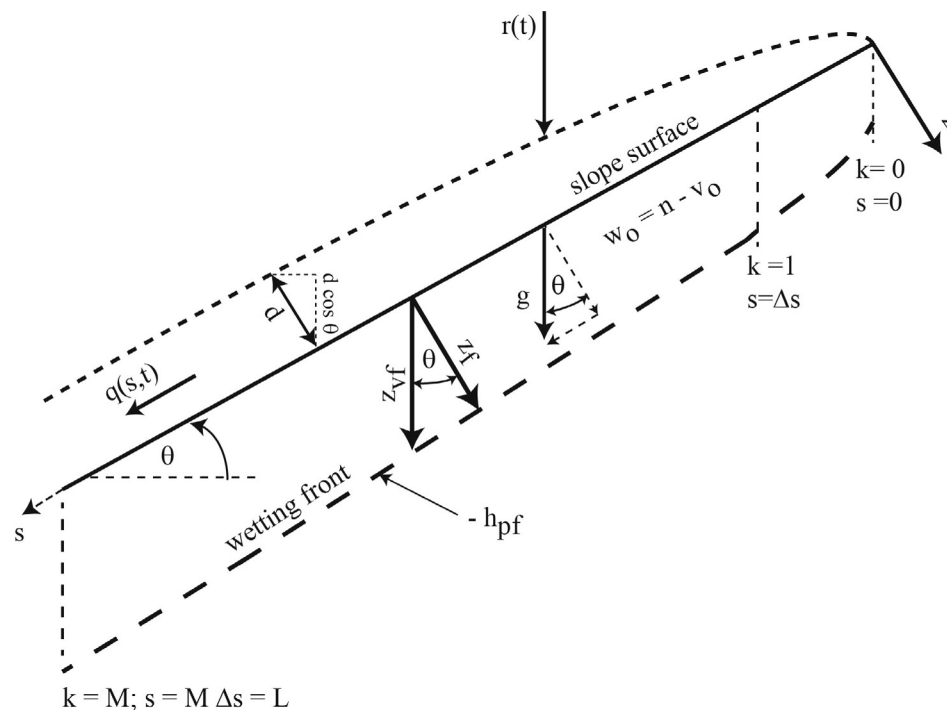


Fig. 1. Schematic of the variables describing runoff and infiltration on a slope (elevation view not drawn to scale).

$$z_f = \frac{G}{n-v_\phi} \cos \theta \quad (2)$$

The soil–water tension along the wetting front is denoted by h_{pf} (units of length) in Fig. 1. The soil–water tension equals the negative of the pore pressure head along the wetting front, and, thus, is a positively valued variable given that the pore pressure in unsaturated soil is negative (i.e., less than atmospheric). The soil water tension on the wetting front h_{pf} is a hydraulic characteristic that varies with soil texture (see, e.g., Rawls and Brakensiek, 1983; Rawls et al., 1992).

This work introduces a modified version of the classic Green and Ampt infiltration model (see [Green and Ampt, 1911](#)) applicable to sloping terrain subjected to time-variable surficial wetting. A review of the Green and Ampt model (the G&A model, henceforth) and its underlying assumptions can be found in [Dingman \(2015\)](#), among others. This work's modified G&A model calculates coupled infiltration and runoff on sloping terrain, and resolves the effect of infiltration depth on slope stability. Furthermore, this paper presents the 1D pde describing the combined erosive power of slope runoff and infiltration. The erosion rate is expressed as function of the runoff rate, infiltration rate, and suspended-sediment concentration under approximate steady-state conditions. The simultaneous calculation of slope wetting, infiltration, runoff, and erosion constitutes this paper's theoretical novelty. The numerical algorithms for the calculation of slope infiltration, runoff, and slope stability constitute the practical result of this paper's theory. The original G&A infiltration model estimates the infiltration in a homogeneous and isotropic soil underlying level ground. The classic G&A model has been implemented by several authors (see, e.g., [Mein and Larson, 1973](#); [Morel-Seytoux, 1980](#); [Hydrologic Engineering Center, 2000](#)). [Chen and Young \(2006\)](#) reported a model for G&A infiltration in sloping surfaces. The latter work did not address the effect of infiltration on slope stability and slope degradation, as this paper does. The G&A model has been shown to comply well with the Richards equation results under the model assumptions ([Salvucci and Entekhabi, 1995](#)). [Loáiciga \(2005\)](#) reported calculation of groundwater recharge to sloping aquifers. [Loáiciga and Huang \(2007\)](#) presented a G&A infiltration model that accounted for temporally variable rainfall with interspersed dry periods in which the ponding depth was depleted by

infiltration and evaporation. Several authors have reported simulations of surface flow affected by infiltration on sloping terrain relying on models other than the G&A formulation. [Strelkoff and Clemmens \(1994\)](#), for example, calculated surface flow in sloping-border irrigation by solving the Saint Venant equations with infiltration described by Kostiakov's formula. [Bradford and Katopodes \(2001\)](#) presented a finite-volume model for unsteady, two-dimensional, shallow water flow to simulate the advance and infiltration of an irrigation wave in non-level basins. [Wöhling et al. \(2004\)](#) reported a surface–subsurface flow model for furrow irrigation employing the Hydrus 2D model for subsurface simulation of water flow. [Zerihun et al. \(2005\)](#) developed a hydraulic model coupled to a surface model (Hydrus 1D) for flow and solute transport in irrigation borders and basins. The four latter publications on irrigation models did not address slope stability by soil wetting. [Weill et al. \(2009\)](#) reported a numerical model for coupled surface and subsurface flow simulation with the objective of elucidating water dynamics in catchments with consideration to the surface/subsurface interface employing a generalized Richards equation. Their model was not concerned with the analysis of slope stability or erosion caused by slope wetting. [Morbidei et al. \(2018\)](#) presented a review of research dealing with infiltration on sloping terrain.

This paper's contribution is the development of the G&A model for infiltration on sloping ground coupled with kinematic-wave modeling of runoff. The infiltration-runoff model solves the coupled equations of runoff and infiltration driven by time-variable water input on sloping terrain. This paper generalizes the work of [Johnson and Loáiciga \(2017\)](#) by considering the existence of lateral subsurface flow downslope, by applying a time-variable upstream boundary condition (at $s = 0$) for infiltration that accounts for the temporal evolution of soil wetting at the slope crown, and by elucidating the effect of infiltration on slope erosion. Centrally, this paper resolves the effect an advancing wetting front has on reducing the factor of safety (FS) against translational sliding in sloping terrain formed by cohesive or cohesionless soils. Our work generalizes the slope sliding model by [Iverson \(2000\)](#) by jointly simulating infiltration and slope runoff and accounting for their combined effect on translational slope stability. This paper's analytical and numerical methods complement experimental research of infiltration in sloping terrain ([Morbideilli et al., 2015, 2016](#)). Lastly, this work

develops the pde governing suspended sediment continuity and submerged slope degradation caused by external wetting and influenced by infiltration.

Section 2 presents the geometric setting, hydrologic methods, and numerical algorithms employed in this paper. Section 3 summarizes this paper's results. Section 4 outlines extensions to the theory presented in Section 2. The extensions cover linearly variable antecedent water content, and the development of the partial differential equations governing suspended-sediment concentration, runoff, infiltration, and slope degradation. Section 5 (Conclusion) summarizes this paper's key findings. The Appendix A develops the 2D Richards equation for unsaturated soil in arbitrarily rotated Cartesian coordinates. All the symbols employed in this paper are listed in Section 6 (Symbology). A list of bibliographic references is found in the References section.

2. Theory and methods

2.1. The G&A infiltration equation in sloping terrain

This section develops a G&A infiltration model for sloping terrain. Prior to the initiation of runoff at time t_Q infiltration equals the cumulative water input (R):

$$G(s, t) = R(t) \quad 0 \leq t \leq t_Q; 0 \leq s \leq L \quad (3)$$

Once runoff begins a positive pressure head ($=d \cos \theta$ in Fig. 1) forms on the slope surface ($z = 0$), which gives rise to simultaneous and coupled infiltration and runoff.

Fig. 2 depicts a representative elementary volume ABCD (REV) whose sides are oriented parallel to the axes s and z introduced in Fig. 1.

The third dimension of the REV shown in Fig. 2 is unitary and perpendicular to the s and z axes. The hydraulic head (h) within the REV is defined with respect to a datum on which the elevation head $z_v = 0$, and z_v increases in magnitude in a downward direction as shown in Fig. 2. The pressure head within the REV is negative given that it is partially saturated. The pressure head within the REV is denoted by $-h_p$, in which h_p represents the soil–water tension (positive, in m). The hydraulic head within the REV equals $h = -z_v - h_p$. This choice of variables and the geometry of Fig. 2 imply that $\Delta z_v / \Delta s = \cos \theta$ and $\Delta z_v / \Delta z = \sin \theta$. It follows that in the limit (as Δs , Δz , and $\Delta z_v \rightarrow 0$) the Darcian fluxes q_s and q_z along the axes s and z , respectively are given by the following equations:

$$q_s = -K \frac{\partial h}{\partial s} = K \sin \theta + K \frac{\partial h_p}{\partial s} \quad (4)$$

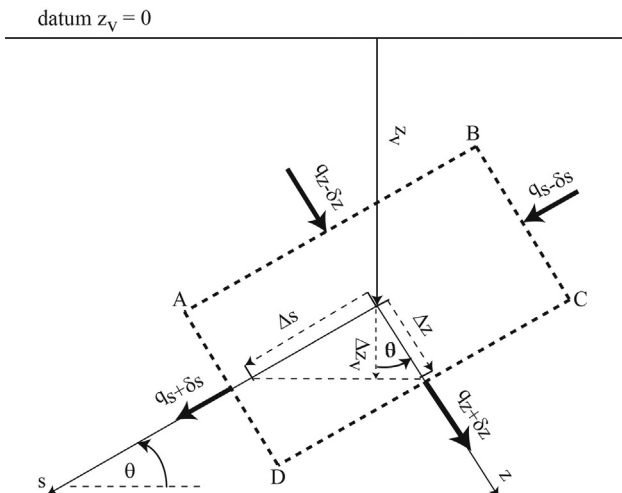


Fig. 2. A representative elementary REV of slope soil (elevation view not drawn to scale).

$$q_z = -K \frac{\partial h}{\partial z} = K \cos \theta + K \frac{\partial h_p}{\partial z} \quad (5)$$

in which K denotes the soil's hydraulic conductivity. The unsaturated hydraulic conductivity can be expressed in terms of the volumetric water content according to the soil's moisture-conductivity curve. Alternatively, the unsaturated hydraulic conductivity is expressible as a function of the soil–water tension relying on the soil's moisture-characteristic curve (Brooks and Corey, 1964; Campbell, 1974; van Genuchten, 1980).

The modified G&A infiltration model expresses Eq. (5) for the subsurface water flux perpendicular to the slope in discrete form between the slope surface (where $z = 0$) and the wetting front (where $z = z_f$). The pressure head equals $d \cos \theta$ on the slope surface, and $-h_{pf}$ on the wetting front. Therefore (letting K_o denote the saturated hydraulic conductivity), the Darcian flux along coordinate z is given by:

$$q_z = K_o \cos \theta + K_o \left(\frac{d \cos \theta + h_{pf}}{z_f} \right) \quad (6)$$

The infiltration rate along the z coordinate equals $g \cos \theta$, which equals the Darcian flux given by Eq. (6). Furthermore, the infiltration rate equals the time derivative of the infiltration G . Eq. (6) is valid after the time (t_Q) when runoff begins and generates a positive pressure head on the slope surface. The G&A formulation of the Darcian flux in Eq. (6) assumes a “piston”-like advance of the wetting front, with the pressure head varying between $d \cos \theta$ on the slope surface and $-h_{pf}$ at the wetting front. The (homogeneous) soil layer of thickness z_f between the slope surface and the wetting front is saturated. These conditions render the G&A model of infiltration quite tractable compared to a formulation based on the exact equation of unsaturated flow (i.e., the 2D Richards equation). The exact formulation of infiltration on sloping terrain raises several complex issues concerning the calculation of the time to runoff initiation and the formulation of boundary conditions of the subsurface flow domain that do not arise with the G&A model. The Appendix A presents an analysis of the 2D Richards equation of unsaturated flow in rotated coordinates, and explains the complexities that arise in solving simultaneously the runoff and infiltration equations with the exact formulation.

Eq. (6) is rewritten in terms of the infiltration (G), employing Eq. (2) to express z_f , and leveraging the fact that q_z equals $g \cos \theta = (\partial G / \partial t) \cos \theta$:

$$\frac{\partial G(s, t)}{\partial t} \cos \theta = K_o \cos \theta + K_o \left(\frac{d(s, t) \cdot \cos \theta + h_{pf}}{\frac{G(s, t)}{n - v_0} \cos \theta} \right) \quad (7)$$

Eq. (7) is rewritten as a conventional partial differential equation:

$$G \frac{\partial G}{\partial t} - K_o G - a_0 d - a_1 = 0 \quad t > t_Q; 0 \leq s \leq L \quad (8)$$

where

$$a_0 = \frac{K_o (n - v_0)}{\cos \theta} \quad (9)$$

$$a_1 = \frac{K_o (n - v_0) h_{pf}}{\cos^2 \theta} \quad (10)$$

The initial condition for infiltration is that infiltration equals the cumulative rainfall (or cumulative water input, $R(t_Q)$) at the time when runoff begins (t_Q):

$$G(s, t_Q) = R(t_Q) \quad 0 \leq s \leq L \quad (11)$$

The infiltration increment over a time step equals the amount of rain falling during that period whenever the runoff ceases and rainfall continues to fall. The (upstream) boundary condition for infiltration takes into account that at $s = 0$ the runoff depth (d) equals zero. Therefore, setting $d = 0$ in Eq. (8) permits writing the infiltration

boundary condition in the following form that is useful for its numerical integration:

$$\frac{\partial G(0,t)}{\partial t} = K_o + \frac{a_1}{G(0,t)} \quad t > t_Q \quad (12)$$

Eq. (12) expressing the boundary condition for infiltration is integrated by separation of variables to yield the following implicit relation between time and infiltration:

$$t - t_Q = \frac{G(0,t) - R(t_Q)}{K_o} - \frac{a_1}{K_o^2} \ln \left(\frac{K_o G(0,t) + a_1}{K_o R(t_Q) + a_1} \right) \quad t > t_Q \quad (13)$$

Eq. (12) is the preferred formulation of the boundary condition for the purpose of numerical solution of the infiltration problem. It is worthy of mention that the G&A formulation of infiltration with water application on a slope involves simple flow-domain geometry (depicted in Fig. 1) and mathematical description of the boundary condition. No assumption is necessary for a phreatic surface beneath the wetting front.

Eqs. (8)–(12) summarize the mathematical statement for infiltration on sloping terrain. Eq. (8) involves the unknown runoff depth. A second equation is needed for the runoff depth, which is derived employing kinematic-wave theory in the **Kinematic wave runoff** section. A key variable for slope stability analysis is the depth to the wetting front, which is calculated with either Eqs. (1) or (2) once the infiltration is resolved.

2.2. The time to the initiation of slope runoff (t_Q)

The time required to initiate slope runoff (t_Q) is defined by the instant in which the component of the rainfall rate (or water-input rate, in general) along the coordinate z first equals the infiltration rate along that same coordinate. Employing Eq. (7) (with $d = 0$) we have:

$$r(t_Q) \cos \theta = K_o \cos \theta + K_o \cdot \left(\frac{h_{pf}}{\frac{R(t_Q)}{n - v_o} \cos \theta} \right) \quad (14)$$

in which $R(t_Q)$ denotes the cumulative rainfall at time t_Q . Eq. (14) must be solved numerically for most instances of variable water input. The case of constant water input r_o leads to a closed-form solution for t_Q :

$$t_Q = \frac{1}{r_o} \cdot \frac{K_o h_{pf} \cdot (n - v_o)}{(r_o - K_o) \cos^2 \theta} \quad (15)$$

where the (constant) water input (r_o) must exceed the saturated hydraulic conductivity (K_o) to obtain physically meaningful results. Another case of interest in this work is that of a symmetric triangular water-input rate over a duration D , as shown in Fig. 3. In Fig. 3 the rising limb of the water-input rate is expressed as $r = c \cdot t$. In this case the time t_Q is the smallest root (positive and real valued) of the following third-order polynomial:

$$b_0 t^3 + b_1 t^2 + b_2 = 0 \quad (16)$$

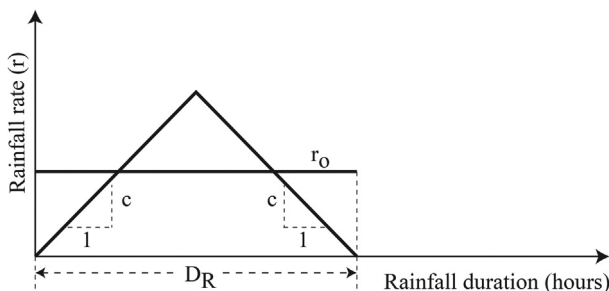


Fig. 3. Constant (r_o) and triangular rainfall rates lasting D_R hours and producing the same depth of rain ($r_o D_R$).

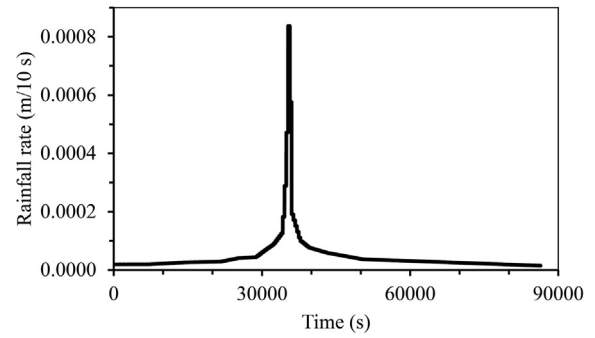


Fig. 4. NRCS type I, 24-h, rainfall hyetograph scaled to a total depth equal to 0.400 m.

where $b_0 = c^2 \cos^2 \theta$, $b_1 = -c K_o \cos^2 \theta$, $b_2 = -2 K_o h_{pf} \cdot (n - v_o)$.

Determining the time (t_Q) for rainfall rates specified as a time series of discrete values of rain depth (r_d) each occurring over a computational time period (Δt) requires a numerical solution of Eq. (14).

Fig. 4 depicts the United States Department of Agricultural's Natural Resources Conservation Service (NRCS) 24-h, Type I, rainfall hyetograph, in this case scaled to produce a depth of rain equal to 0.400 m. Notice the high intensity of rainfall near half the duration of the storm.

Letting the index j denote the counter for time intervals, $j = 1, 2, \dots, T$, the cumulative rain at time $j \Delta t$ is calculated as follows:

$$R(j \Delta t) = \sum_{l=1}^j r_d(l \Delta t) \quad (17)$$

The discrete form of Eq. (14) applied to estimate the time t_Q takes the form:

$$r_d(j \Delta t) = \Delta t \cdot \left[K_o + K_o \cdot \left(\frac{h_{pf}}{\frac{R(j \Delta t)}{n - v_o} \cos^2 \theta} \right) \right] \quad (18)$$

The value j that satisfies Eq. (18) for the first time is denoted by j_Q , and the time of runoff initiation is given by $t_Q = j_Q \cdot \Delta t$.

2.3. Kinematic wave runoff

Runoff on a slope surface is wide and shallow resulting in a hydraulic radius approximately equal to the depth of runoff d . This permits the application of the kinematic-wave approximation to the flow equation on a slope. Runoff is herein modeled with the kinematic-wave approximation to the equation of 1-D of overland flow on a slope with accretion by rainfall and depletion by infiltration. The kinematic flow approximation expresses the flow rate as a function of the depth of flow (see, e.g., Chow, 1959; Cunge et al., 1980; Chaudry, 1993; Johnson and Loáiciga, 2017; Singh, 2017). The kinematic-wave flow equation is as follows:

$$\beta \cdot m \cdot d^{m-1} \frac{\partial d}{\partial s} + \frac{\partial d}{\partial t} = r - g = r - G_t \quad (19)$$

in which d denotes the depth of runoff, g and r denote respectively the infiltration rate and rainfall rate, and the derivative of the infiltration G with respect to time is represented by G_t ($= g$). The coefficient $m = 5/3$, and β is defined as:

$$\beta = \frac{1}{N} \cdot \sqrt{S_0} \quad (20)$$

where N and S_0 denote the Manning's roughness coefficient and the slope of the terrain, respectively. The initial condition of Eq. (19) is defined as follows:

$$d(s, t = t_Q) = 0 \quad 0 \leq s \leq L \quad (21)$$

in which t_Q denotes the time when runoff emerges on the slope. The depth of runoff equals zero prior to the time t_Q . The boundary condition

of Eq. (19) at the upstream end is given by:

$$d(s = 0, t) = 0 \quad t \geq t_Q \quad (22)$$

The overland flow $q(s, t)$ (in m^3/s) at location s and time t is given by Manning's equation:

$$q(s, t) = \frac{1}{N} \cdot \sqrt{S_0} \cdot b \cdot (d(s, t))^{\frac{5}{3}} \quad (23)$$

The following section introduces a numerical method for the joint solution of the infiltration and runoff equations outlined above.

2.4. Numerical solution of the infiltration and runoff equations

2.4.1. Explicit finite-difference formulation of the infiltration equation

The flow domain has $M + 1$ nodes with an inter-nodal separation equal to Δs , as shown in Fig. 1. The nodal index equals $k = 0, 1, 2, 3, \dots, M$. The node at $k = 0$ corresponds to the upstream boundary, where the value of runoff depth equals zero. The time domain is divided into a computational time step Δt , with time index $j = 1, 2, \dots, T$. The finite-difference, explicit, numerical discretization of the infiltration Eq. (8) applied in this work is given by the following expression:

$$\left(\frac{G_k^{(j-1)} + G_{k-1}^{(j-1)}}{2} \right) \left(\frac{G_k^{(j)} - G_{k-1}^{(j-1)}}{\Delta t} \right) - K_o \cdot \left(\frac{G_k^{(j-1)} + G_{k-1}^{(j-1)}}{2} \right) - a_0 \cdot \left(\frac{d_k^{(j)} + d_{k-1}^{(j-1)}}{2} \right) - a_1 = 0 \quad (24)$$

$k = 1, 2, 3, \dots, M$, and $j = j_Q + 1, j_Q + 2, j_Q + 3, \dots$, where $t_Q = j_Q \cdot \Delta t$ represents the time of runoff initiation. The indexed notation applied in Eq. (24) is such that:

$$G_{k-1}^{(j-1)} = G((k-1) \cdot \Delta s, (j-1) \cdot \Delta t) \quad (25)$$

$$G_k^{(j-1)} = G(k \cdot \Delta s, (j-1) \cdot \Delta t) \quad (26)$$

$$G_k^{(j)} = G(k \cdot \Delta s, j \cdot \Delta t) \quad (27)$$

$$d_k^{(j)} = d(k \Delta s, j \Delta t) \quad (28)$$

$$d_k^{(j-1)} = d(k \Delta s, (j-1) \Delta t) \quad (29)$$

The initial condition associated with Eq. (24) is given by the following formula:

$$G_k^{(j_Q)} = R(t_Q) \quad (30)$$

$k = 0, 1, 2, 3, \dots, M$. The boundary condition of Eq. (24) is the discretized form of Eq. (12) (at $k = 0$):

$$G_0^{(j)} = G_0^{(j-1)} + K_o \cdot \Delta t + \frac{a_1 \cdot \Delta t}{G_0^{(j-1)}} \quad (31)$$

in which $j = j_Q + 1, j_Q + 2, j_Q + 3, \dots$

2.4.2. Explicit finite-difference formulation of the kinematic-wave runoff

The kinematic wave pde (19) is a nonlinear hyperbolic pde (Smith, 1984). This paper implements a modified Lax-Wendroff explicit finite-difference method for its solution (see Lax, 1954, and Smith, 1984, for an exposition of the Lax-Wendroff method). The explicit numerical scheme for kinematic wave runoff must meet the following numerical Courant-Friedrichs-Lewy (CFL) stability condition (Courant et al., 1928; Cunge et al., 1980; Smith, 1984; Hydrologic Engineering Center, 2000; Johnson and Loáiciga, 2017):

$$\Delta t \leq \frac{\Delta s}{\sqrt{g^* \cdot d^*}} \quad (32)$$

in which g^* equals 981 cm/s^2 , and represents the acceleration of gravity, and d^* denotes an average depth of runoff. The selection of Δt and Δs must be made judiciously to satisfy Eq. (32). Thus, for example, Δs may be set equal to 100 cm (1 m) to calculate runoff depth and

infiltration with adequate spatial resolution, in which case by virtue of Eq. (32) Δt may not exceed 1.4 s for an average runoff depth $d^* = 5 \text{ cm}$. The explicit finite-difference formulation of the kinematic-wave runoff equation is relatively simple, and it is stable and accurate when the condition (32) is met and a suitable inter-nodal computational step is chosen. It is obtained by discretizing Eq. (19) (the node at $k = 0$ corresponds to the upstream boundary, where the value of runoff depth equals zero):

$$\frac{d_k^{(j)} - d_{k-1}^{(j-1)}}{\Delta t} + \beta \cdot m \cdot \left(\frac{d_k^{(j-1)} + d_{k-1}^{(j-1)}}{2} \right)^{m-1} \cdot \left(\frac{d_k^{(j-1)} - d_{k-1}^{(j-1)}}{\Delta s} \right) = r_k^{(j)} - \left(\frac{G_k^{(j)} - G_{k-1}^{(j-1)}}{\Delta t} \right) \quad (33)$$

$k = 1, 2, 3, \dots, M$, and $j = j_Q + 1, j_Q + 2, j_Q + 3, \dots$. The following indexed notation applies to $d_{k-1}^{(j-1)}$ and to the water-application rate (r) in Eq. (33):

$$d_{k-1}^{(j-1)} = d((k-1) \cdot \Delta s, (j-1) \cdot \Delta t) \quad (34)$$

$$r_k^{(j)} = r(j \Delta t) \quad (35)$$

The initial condition associated with Eq. (33) is:

$$d_k^{(j_Q)} = 0 \quad k = 0, 1, 2, 3, \dots, M \quad (36)$$

The upstream boundary condition associated with Eq. (33) specifies zero depth at the slope's crown implying a Dirichlet boundary value problem, whose (upstream) boundary condition is:

$$d_0^{(j)} \equiv 0 \quad j = j_Q + 1, j_Q + 2, j_Q + 3, \dots \quad (37)$$

The kinematic-wave runoff rate is calculated with the following equation:

$$q_k^{(j)} = \frac{1}{N} \cdot \sqrt{S_0} \cdot b \cdot (d_k^{(j)})^{\frac{5}{3}} \quad (38)$$

$k = 1, 2, 3, \dots, M$, and $j = j_Q + 1, j_Q + 2, j_Q + 3, \dots$

2.4.3. Explicit finite-difference solution of the infiltration and kinematic-wave runoff equations

Eqs. (24) and (33) constitute a set of coupled, nonlinear, finite-difference equations involving the unknowns $d_k^{(j)}$ and $G_k^{(j)}$. The discretized infiltration Eq. (24) is rewritten in explicit form for the infiltration in the current time step:

$$G_k^{(j)} = G_k^{(j-1)} + a_{k,k-1}^{(j-1)} \cdot d_k^{(j)} + b_{k,k-1}^{(j-1)} \quad (39)$$

$k = 1, 2, 3, \dots, M$, and $j = j_Q + 1, j_Q + 2, j_Q + 3, \dots$, in which:

$$a_{k,k-1}^{(j-1)} = \frac{a_0}{2G_{k,k-1}^{(j-1)}} \quad (40)$$

$$b_{k,k-1}^{(j-1)} = \frac{G_k^{(j-1)} + G_{k-1}^{(j-1)}}{2\Delta t} \quad (41)$$

$$b_{k,k-1}^{(j-1)} = K_o \Delta t + \frac{a_1}{G_{k,k-1}^{(j-1)}} + \frac{a_0}{G_{k,k-1}^{(j-1)}} \cdot \frac{d_k^{(j-1)}}{2} \quad (42)$$

The runoff depth Eq. (33) is rewritten in explicit form for the current time step:

$$d_k^{(j)} = d_k^{(j-1)} - G_k^{(j)} + f_{k,k-1}^{(j-1)} \quad (43)$$

in which:

$$f_{k,k-1}^{(j-1)} = -x_{k,k-1}^{(j-1)} + r_{d,k}^{(j)} + G_{k-1}^{(j-1)} \quad (44)$$

where $r_{d,k}^{(j)} = r_k^{(j)} \cdot \Delta t$ denotes the depth of water application in time step $j \cdot \Delta t$ at node k .

$$x_{k,k-1}^{(j-1)} = \Delta t \cdot \beta \cdot m \cdot \left(\frac{d_k^{(j-1)} + d_{k-1}^{(j-1)}}{2} \right)^{m-1} \cdot \left(\frac{d_k^{(j-1)} - d_{k-1}^{(j-1)}}{\Delta s} \right) \quad (45)$$

Eq. (39) for $G_k^{(j)}$ is substituted into Eq. (43) to produce an explicit equation for the runoff depth in the j -th computational time step:

$$d_k^{(j)} = h_{k,k-1}^{(j-1)} \cdot d_k^{(j-1)} - h_{k,k-1}^{(j-1)} \cdot G_k^{(j-1)} - h_{k,k-1}^{(j-1)} \cdot b_{k,k-1}^{(j-1)} + h_{k,k-1}^{(j-1)} \cdot f_{k,k-1}^{(j-1)} \quad (46)$$

$k = 1, 2, 3, \dots, M$, and $j = j_Q + 1, j_Q + 2, j_Q + 3, \dots$, (with boundary condition $d_0^{(j)} = 0$) in which:

$$h_{k,k-1}^{(j-1)} = \frac{1}{1 + a_{k,k-1}^{(j-1)}} \quad (47)$$

The runoff depth calculated with Eq. (46) must be non-negative for physical feasibility. The solution algorithm for coupled runoff and infiltration starts by solving Eq. (46) at time step $(j_Q + 1) \cdot \Delta t$. Once the runoff depth has been calculated it is used in Eq. (39) to solve for the infiltration at time step $(j_Q + 1) \cdot \Delta t$. The time index is then increased to $j_Q + 2$ and the consecutive solutions for runoff depth and infiltration are calculated at all active nodes. The solution algorithm is advanced to the third and higher time steps by increasing the time index j by one unit consecutively, solving for infiltration and runoff depth in each time step until reaching the end of the simulation. The ratio $[(\text{Input} - \text{Output}) / (\text{Input})] \times 100$ constitutes the percentage error in mass balance associated with the calculated runoff and infiltration, with Input = cumulative rainfall, and Output = cumulative runoff volume + infiltration. The percentage error measures the accuracy of the numerical solution scheme in preserving balance of inputs and outputs (see, e.g., McDonald and Harbaugh, 1988). The accuracy of the numerical algorithm is evaluated by checking the percentage error in mass balance approaches zero upon termination of the numerical simulation, as shown in the Results section. This paper's simulation algorithm for solving Eqs. (39) and (46) was written in the public-domain software R. The program is accessible at <https://github.com/mikejohnson51/RainSlope> for free download.

2.4.4. The depth to the wetting front

The depth to the wetting front is a key factor controlling slope stability. It is calculated at any node k and time step $j \cdot \Delta t$ with the following equation:

$$z_{vf,k}^{(j)} = \frac{G_k^{(j)}}{n - v_0} \quad (48)$$

in which $k = 0, 1, 2, \dots, M$; $j = 1, 2, 3, \dots$. Notice that for $j = 1, 2, 3, \dots, t_Q$ the infiltration $G_k^{(j)}$ equals the cumulative rainfall $R(j \Delta t)$.

2.5. Slope infiltration and translational slope stability

The classic model for translational slope stability proposes that subsurface water perches over a surface of hydraulic conductivity lower than that of the overlying slope's soil. The surface of hydraulic-conductivity discontinuity is the slip surface along which overlying soil may move downslope causing landslides. The rising thickness of saturation above the slip surface reduces the (frictional) effective stress on that surface and may cause sliding along the slip surface. Descriptions of the classic "infinite" (read "long") slope translational stability model can be found in Duncan et al. (2014) and Loáiciga (2015), among others. However, empirical evidence indicates slopes wetted by rainfall commonly do not feature such zones of conductivity discontinuity. In fact, many translational landslides occur in relatively homogeneous soils driven by the downward advance of saturation, as depicted in Fig. 5, and not by the rise of perched saturation above the slip surface as proposed by the classic model of translational slope stability. It is possible air may be entrapped along the wetting front when there is rapid infiltration, thus hindering the advance of the wetting front, and creating positive pore water pressure through the zone of saturation. It might possible, also, that a reduction in hydraulic conductivity produce a profile of positive pore water pressure through the zone of saturation. These condition is propitious for shallow sliding wherever the advance

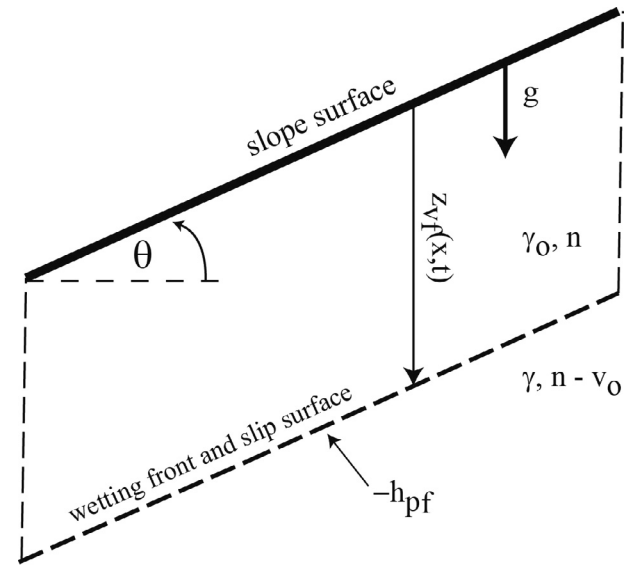


Fig. 5. Schematic of a sliding soil block on a slope. Elevation view not drawn to scale.

of the wetting front is retarded.

This work introduces a method for evaluating translational slope stability considering coupled runoff and infiltration, soil characteristics, and slope geometry. The soil saturated unit weight and the (antecedent) unit weight prior to external wetting are denoted by γ_0 and γ , respectively, as shown in Fig. 5. Let c' and ϕ' denote respectively the effective cohesion and the effective angle of friction of the slope's soil. The ratio of the resisting stress along the slip surface shown in Fig. 5 to the driving stress that often destabilizes the slope along that surface is called the factor of safety (FS). The slope is stable when the factor of safety exceeds 1, is unstable when the factor of safety is less than 1, and is in limiting equilibrium when the factor of safety equals 1. The factor of safety (FS_0) at a depth z_{vf} is determined by force equilibrium and geometric analyses of the soil block depicted in Figure. Prior to infiltration the factor of safety is given by the following expression (in which the pressure head at depth z_{vf} prior to saturation is denoted by $h_{p0} > h_{pf}$):

$$FS_0 = \frac{c'}{z_{vf} \gamma \cos \theta \sin \theta} + \left(1 + \frac{h_{p0}}{z_{vf}} \cdot \frac{\gamma_w}{\gamma} \cdot \frac{1}{\cos^2 \theta} \right) \cdot \frac{\tan \phi'}{\tan \theta} \quad (49)$$

As water infiltrates it changes the water content of the slope's soil. At the advancing wetting front the soil–water tension (at depth z_{vf}) equals h_{pf} and the factor safety equals:

$$FS = \frac{c'}{z_{vf} \gamma_0 \cos \theta \sin \theta} + \left(1 + \frac{h_{pf}}{z_{vf}} \cdot \frac{\gamma_w}{\gamma_0} \cdot \frac{1}{\cos^2 \theta} \right) \cdot \frac{\tan \phi'}{\tan \theta} \quad (50)$$

Eq. (50) demonstrates the factor of safety decreases with increasing depth of the wetting front (z_{vf}). Therefore, the deeper a wetting front driven by infiltration advances, the greater the reduction of the factor of safety would be with concomitant reduction of slope stability. A comparison of Eqs. (49) and (50) demonstrates the factor of safety with infiltration (Eq. (50) is less than that without infiltration for the same depth z_{vf} because Eq. (50) features a larger unit weight (saturated unit weight γ_0) and a smaller soil–water tension (h_{pf}).

Rapid infiltration may trap air in the soil along the wetting front, which may slow down or impede further infiltration. In this instance the water pressure would equal $d \cdot \cos \theta \cdot \gamma_w$ on the slope surface (see Fig. 1) and $(d \cdot \cos \theta + z_{vf} \cos^2 \theta) \cdot \gamma_w$ along the wetting front. This situation may also arise if the hydraulic conductivity is reduced at depth z_{vf} , yet it would be caused by induced saturation from the slope surface downward, rather than by perching of soil water over a soil

discontinuity as assumed in the classic model of slope stability (Loáiciga, 2015). Either one of these two situations is associated with a factor of safety given by:

$$FS = \frac{c'}{z_{yf} \gamma_o \cos \theta \sin \theta} + \left(\frac{\gamma_o - \gamma_w}{\gamma_o} \right) \frac{\tan \phi'}{\tan \theta} \quad (51)$$

From Eq. (51) follows the maximum angle a slope of cohesionless soil ($c' = 0$) may have and be stable:

$$\theta = \tan^{-1} \left(\left(\frac{\gamma_o - \gamma_w}{\gamma_o} \right) \cdot \tan \phi' \right) \quad (52)$$

Eq. (52) states the maximum angle natural or constructed slopes may have when induced soil saturation produces air trapping along the wetting front or a reduction of hydraulic conductivity occurs at any depth.

The Results section offers examples of the effect of infiltration on translational slope stability.

3. Results

3.1. Cohesive soil

The first example illustrates this paper's theory with a cohesive soil (with negligible friction strength) whose factor of safety against sliding is given by the first term of the right-hand side of eq. (50). Two 24-h storms were employed in separate applications of this paper's runoff-infiltration method and slope stability analysis. Table 1 lists the slope geometry and hydraulic parameters applied in this example. The spatial computation step was set to $\Delta s = 1$ m, and the time step $\Delta t = 1$ s. Numerical calculations were also conducted with combinations of Δs and Δt that satisfied the CFL stability condition (32), while keeping Δs less than 2 m. The numerical simulation produced identical results with all chosen combinations of Δs and Δt . Two distinct rainfall distributions were employed, one of the storms had a constant intensity yielding a total depth of 0.400 m over 24 h (see diagram in Fig. 3, with the rainfall rate $r_0 = 4.63 \times 10^{-6}$ m/s). The other storm features a symmetric triangular rainfall rate as depicted in Fig. 3 (with the slope coefficient in Fig. 3 having magnitude $\pm 2.14335 \times 10^{-10}$ m/s² in the rising and recession limbs, respectively) also yielding 0.400 m of rain over 24 h.

Table 2 lists the cohesive soil's characteristics used in this example, which in this case are the porosity (n), (volumetric) water content (v_0), water tension at the wetting front (h_{pf}), hydraulic conductivity (K_0) effective cohesion (c'), and saturated unit weight (γ_o).

Fig. 6 illustrates the determination of the time of runoff initiation (t_Q) corresponding to the constant rainfall rate; t_Q equals 3610 s in this case, which is the time when the rainfall rate equals the infiltration rate. Notice the relatively high rate of infiltration at early time.

Fig. 7 displays the diagram illustrating the determination of the time of runoff initiation associated with the triangular rainfall rate, in which case $t_Q = 15,858$ s. It is seen in Fig. 7 the constant rainfall rate generates runoff at a much earlier time ($t_Q = 3610$ s) than the symmetric triangular rainfall rate. It is seen in Fig. 7 the relatively high value of the infiltration rate at early time.

Fig. 8 displays the variation of the runoff depth calculated for various times since the beginning of constant rainfall that delivers 0.400 m of water in 24 h. The graphs shown in Fig. 8 demonstrate the runoff

Table 2

Cohesive soil properties.

| Porosity (n) | Water content (v_0) | Water tension (h_{pf} , m) | Conductivity (K_0 , m/s) | Cohesion (c' , kN/m ²) | Unit weight (γ_o , kN/m ³) |
|------------------|-------------------------|-------------------------------|-----------------------------|---------------------------------------|--|
| 0.30 | 0.15 | 0.25 | 1.39×10^{-6} | 10 | 20 |

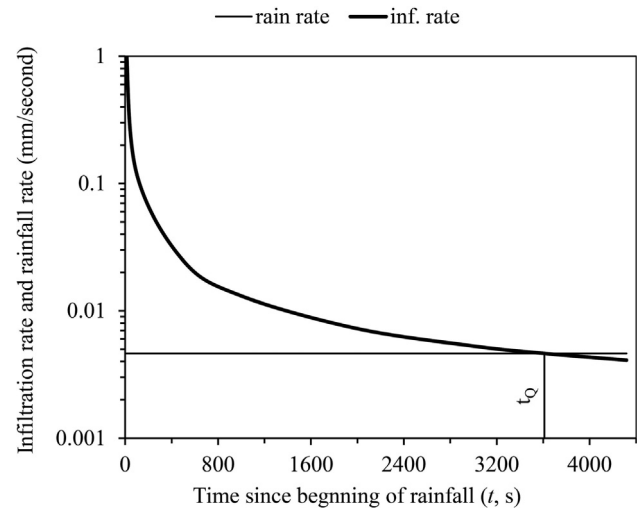


Fig. 6. Graphical determination of the time of runoff initiation (constant rainfall).

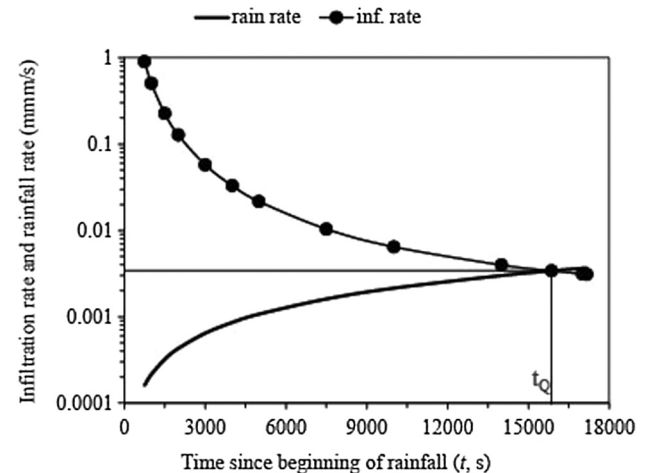


Fig. 7. Graphical determination of the time of runoff initiation (symmetric triangular rainfall).

depth converges to a steady state after 1365 min of uniform rainfall, and so does the runoff rate because it is a function of the depth in the kinematic wave formulation (see Eq. (23)). The infiltration rate corresponding to the runoff depth that approaches steady state is derived from Eq. (8) to yield the following expression (when $d(s,t) \rightarrow d(s)$):

$$g(s,t) = K_0 + \frac{a_0 d(s) + a_1}{G(s,t)} \quad (53)$$

Fig. 9 displays the calculated runoff depth (d) associated with the constant and triangular symmetric rainfall rates. The runoff depth was calculated at the toe of the slope ($s = L = 300$ m), where it reaches its maximum magnitude. It is seen in Fig. 9 the earlier appearance of runoff produced by the constant rainfall rate. The runoff depth produced by constant rainfall increases rapidly until the time when the

Table 1

Slope geometry and runoff data for first example of slope stability.

| Slope and slope angle (S_0, θ) | Roughness coeff. (N) | Length (L , m) | Width (b , m) | Rainfall (r , m) |
|---|--------------------------|-------------------|------------------|---|
| 5H:1V ($\theta = 11.31^\circ$) | 0.20 | 300 | 50 | 0.400 m constant or triangular (Fig. 3) |

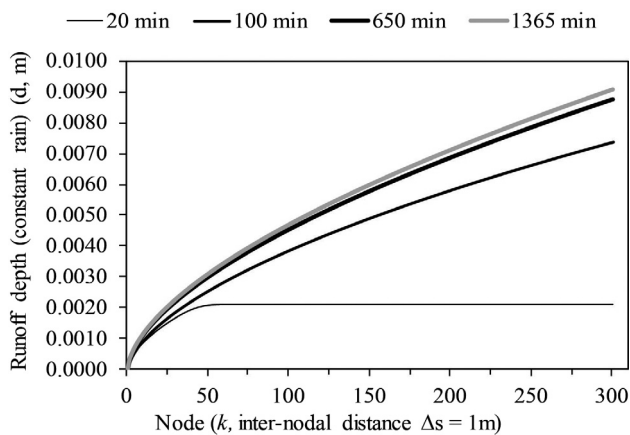


Fig. 8. Runoff depth on the slope for various times since the beginning of constant rainfall.

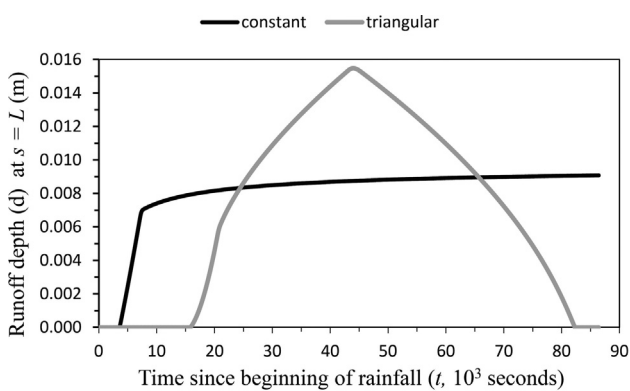


Fig. 9. Runoff depth at the slope toe ($s = L = 300$ m) caused by constant and triangular rainfall rates.

entire slope is contributing to runoff at the toe of slope, which happens at about 9000 s when the runoff depth is about 7 mm. Thereafter, the runoff depth increases slowly from about 7 mm to about 9 mm of depth at the end of the rainfall event (24 h = 86,400 s). The graph of runoff depth corresponding to the triangular rainfall indicates the rate of increase of the runoff depth is largest between 0 and 20,600 s, peaking at the latter time, when the runoff depth equals 5.7 mm. At this time the entire slope is contributing runoff to the slope's toe.

The runoff depth caused by the triangular rainfall increases until reaching a maximum at about 44,000 s, when it equals about 15.5 mm at the slope's toe. Thereafter, it decreases to a nil value at 82,400 s. The overall shapes of the runoff-depth diagrams associated with the constant and triangular rainfalls at all other locations along the slope ($0 < s < L$) are similar to those depicted in Fig. 9, but with the depth (d) progressively scaled down as each approaches the upstream boundary (where $d = 0$ for all times).

Fig. 10 displays the calculated depth to the wetting front associated with the constant and triangular rainfalls. The depths to the wetting front were calculated at the times of initiation of runoff (t_Q) corresponding to the constant and triangular rainfalls, which were 3610 and 15,858 s, respectively, and at the end of rainfall (86,400 s). The depth to the wetting front at the end of rainfall is of special importance because it represents the critical condition for slope stability, as shown below.

Fig. 10 indicates the depth to the wetting front is fairly uniform along the slope, reaching its largest magnitude at the slope toe. The depths to the wetting fronts associated with constant rainfall and triangular rainfall at the slope toe equal 1.30 and 1.13, respectively. Evidently, infiltration is more effective when the water application rate is constant, all other factors being equal. Therefore, the constant

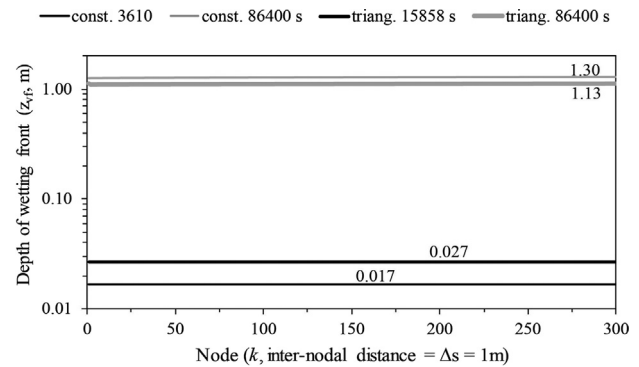


Fig. 10. Calculated depths to the wetting fronts corresponding to the constant and triangular rates at the initiation of runoff and at the end of rainfall.

rainfall poses a greater hazard to slope stability than the triangular rainfall due to its deeper penetration depth. The percentage error in mass balance was less than 0.1% in this example, which demonstrates the accuracy of the calculated infiltration and cumulative runoff.

The factor of safety shown in Fig. 11 was calculated with the first term on the right-hand side of Eq. (50) for a soil exhibiting cohesive strength only, which, as listed in Table 2 is typical of a very soft cohesive soil ($c' = 10$ kN/m² in this example). Nevertheless, the results of Fig. 11 indicate this slope would remain stable when the wetting front reaches its maximum value equal to 1.30 m, which has a corresponding factor of safety equal to 2. The factor of safety was extrapolated to a depth of the wetting front equal to 2.60 m in Fig. 11, which is the depth the wetting front would need to penetrate to cause a translational slide. The results from this example establish that translational slides are unlikely to occur even in soft cohesive soils by external wetting, unless the soil is sensitive and its structure collapses under wetting. Cohesive homogeneous soils are more prone to fail along circular or logarithmic spiraled, deep-seated, slip surfaces (Lambe and Whitman, 1969; Griffiths and Marquez, 2007; Duncan et al., 2014; Loáiciga, 2015).

3.2. Cohesionless soil

Cohesionless soils (effective cohesion $c' = 0$) are known to be prone to translational sliding by rainfall wetting (Cedegren, 1989; Loáiciga, 2015), and they cause substantial loss of life and property annually the world over (see, e.g., Schuster et al., 2002). The factor of safety against sliding of a cohesionless soil is given by the second term on the right-hand side of Eq. (50). The calculation of coupled runoff and infiltration and their effect on slope stability is illustrated in this second example relying on the NRCS 24-h, Type I, rainfall hyetograph scaled to a total depth of rainfall equal to 0.400 m, shown in Fig. 4.

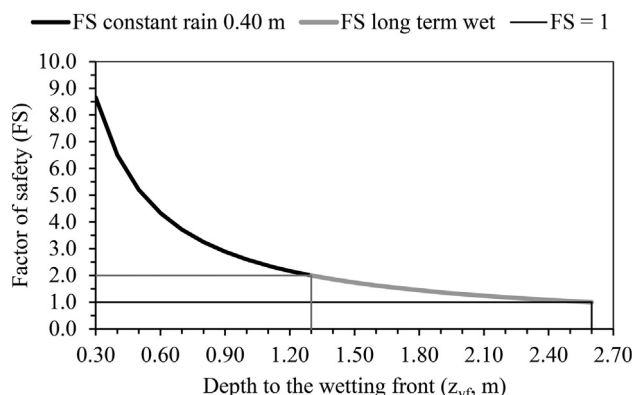


Fig. 11. The factor of safety (FS) for slope stability associated with constant rainfall.

Table 3
Slope geometry and runoff data used in the second example of slope stability.

| Slope and slope angle (S_0, θ) | Roughness coeff. (N) | Length (L , m) | Width (b , m) | Rainfall (r , m) |
|---|--------------------------|-------------------|------------------|------------------------------------|
| 1.2H:1V ($\theta = 39.81^\circ$) | 0.20 | 300 | 50 | 0.400 m NRCS Type I, 24-h (Fig. 4) |

Table 4
Cohesionless soil properties.

| Porosity (n) | Water content (v_0) | Water tension (h_{pf} , m) | Conductivity (K_0 , m/s) | Friction angle (ϕ') | Unit weight (γ_0 , kN/m ³) |
|------------------|-------------------------|-------------------------------|-----------------------------|----------------------------|--|
| 0.30 | 0.15 | 0.15 | 1.39×10^{-5} | 35 | 20 |

Table 3 lists the hydraulic and geometric properties applied in this second example, in which the computational steps Δs and Δt were set to 10 m and 10 s, respectively. Numerical calculations were also conducted with combinations of Δs and Δt that satisfied the CFL stability condition (32), while keeping Δs less than 10 m. Numerical simulations produced identical results with all chosen combinations of Δs and Δt .

The slope used in this second example is steeper than in the first example. Table 4 lists the cohesionless soil's properties applied in this example, which in this case are the porosity (n), (volumetric) water content (v_0), water tension at the wetting front (h_{pf}), hydraulic conductivity (K_0), effective friction angle (ϕ'), and saturated unit weight (γ_0).

One remarkable feature of the cohesionless soil employed in this example is that it is ten times more permeable than the cohesive soil of the first example (compare the K_0 values in Tables 2 and 4). The friction angle of the cohesionless soil (35°) is less than the slope angle (39.81°) meaning the cohesionless soil is stable so long as the friction stress induced by soil–water tension is sufficient to overcome the deficit of frictional strength that would occur on the same dry slope with the given geometric characteristics.

Fig. 12 displays the time history of the rainfall rate, infiltration rate, the time of initiation of runoff ($t_Q = 34,740$ s), and the infiltration (G) at the slope toe. It is evident the duration of excess rainfall generating runoff is short lived, starting at the time of initiation of runoff ($t_Q = 34,740$ s). The infiltration at the slope toe equals 0.326 m at the end of rainfall, meaning 0.074 m of the total rainfall ($= 0.400$ m) drains

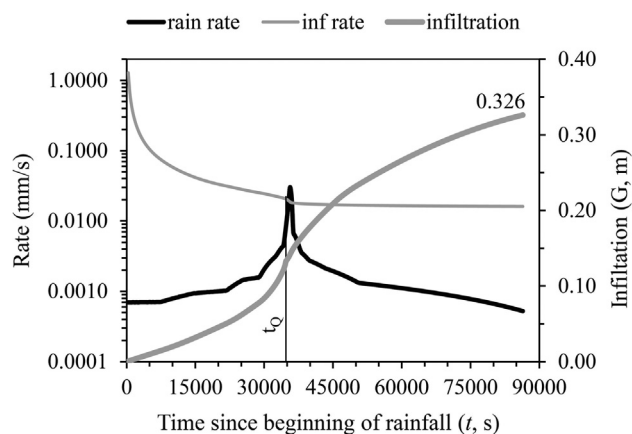


Fig. 12. Rainfall rate, infiltration rate, the time of initiation of runoff (t_Q), and the infiltration associated with the NRCS type I storm event.

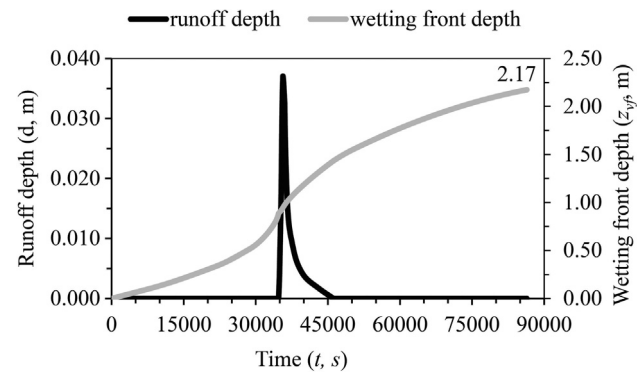


Fig. 13. The runoff depth and the depth to the wetting front calculated at the slope toe and corresponding to the NRCS type I storm event.

from the slope as runoff at that location.

Fig. 13 displays the calculated runoff depth (d) and the depth to the wetting front at the toe of the slope (z_{wf}). Runoff begins at time 34,740 s and ends at 46,630 s at this location. This is the time interval when rainfall is most intense, which causes the wetting front to advance at its fastest rate during the 24-h period of rainfall. The depth to the wetting front reached a maximum equal to 2.17 m. The calculated percentage error in mass balance was less than 0.1% in this example, proving the accuracy of the numerical algorithm.

Fig. 14 depicts the factor of safety (FS) calculated for the cohesionless soil with properties listed in Table 4.

The factor of safety graphed in Fig. 14 was calculated with the second term on the right-hand side (the frictional term) of Eq. (50). It is evident from Fig. 14 the slope would fail in this case when the depth to the wetting front reaches 0.65 m, which corresponds to 0.0975 m of infiltration ($= 0.65 \times 0.15$, where 0.15 equals the water-content deficit $n - v_0$). This shows permeable soil receiving rainfall depth on the order of 0.0975 m could experience sliding.

Eq. (52) can be employed to calculate the maximum slope angle for which slope stability is maintained when the advance of the wetting front is impeded by compressed air or a reduction of hydraulic conductivity at any depth thus causing positive pressure from the slope surface through the wetting front. Using a saturated unit weight equal to 20 kN/m³ and angle of effective friction equal to 35° as before, it is determined the maximum angle the slope may have to be stable equals 19.6° .

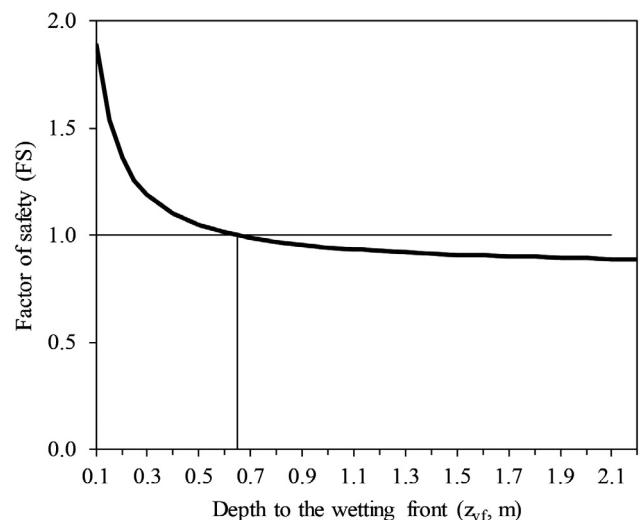


Fig. 14. Factor of safety for the example involving a cohesionless soil.

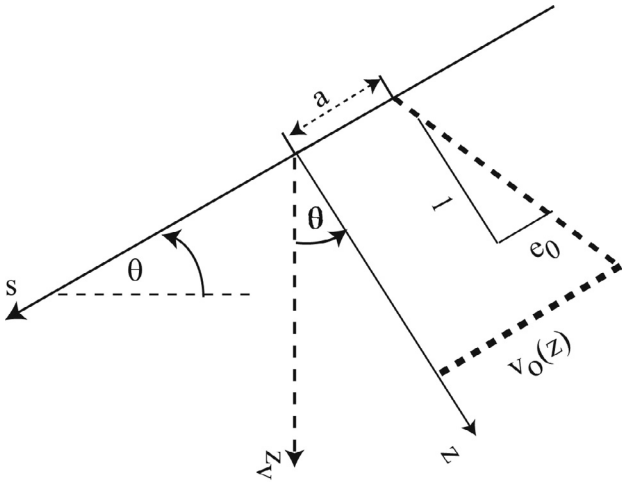


Fig. 15. Diagram of a linearly variable antecedent water content (elevation view not drawn to scale).

4. Extensions of this paper's theory

4.1. Linearly variable antecedent (volumetric) water content

The theory presented in this work assumes a constant antecedent volumetric water content (v_0). This section describes an extension of this paper's theory to include an antecedent water content that varies linearly with depth, as shown in Fig. 15. The antecedent volumetric water content (v_0) is given by the following expression:

$$v_0(z) = a + e_0 \cdot z \quad (54)$$

in which the coefficients a and e_0 describe the variation of the antecedent water content with depth as depicted in Fig. 15. The antecedent water content v_0 increases (or decreases) with increasing depth (z) when the coefficient e_0 is positive (or negative).

The component of infiltration along the axes equals the integral of the water-content deficit from the slope surface to the depth of the wetting front (z_f):

$$G \cos \theta = \int_{z=0}^{z_f} (n - v_0(z)) dz = (n - a) \cdot z_f - \frac{e}{2} z_f^2 \quad (55)$$

Substituting Eq. (54) into Eq. (7) produces the following partial differential equation for the depth to the wetting front:

$$((n - a) - e \cdot z_f) \cdot z_f \frac{\partial z_f}{\partial t} - (K_o \cos \theta) \cdot z_f - K_o \cdot (d(s, t) \cdot \cos \theta + h_{pf}) = 0 \quad (56)$$

By solving Eq. (56) (numerically) for $z_f(s, t)$ one can obtain the infiltration from Eq. (55):

$$G(s, t) = \frac{1}{\cos \theta} \left[(n - a) \cdot z_f - \frac{e}{2} z_f^2 \right] \quad (57)$$

Eq. (56) involves the runoff depth ($d(s, t)$). The numerical solution of Eqs. (56) and (57) for infiltration, and of Eq. (19) for the runoff depth proceeds similarly to the explicit-finite difference algorithm described in this paper for the case when $e = 0$ (i.e., constant antecedent water-content deficit ($n - v_0$)).

The calculation of the time to the initiation of runoff (t_Q) when the antecedent water content varies linearly with depth is needed to solve the runoff and infiltration equations. Recall slope runoff begins when the rainfall rate first equals the infiltration rate and exceeds it immediately thereafter. This condition is determined resorting to Eq. (6) to yield the following equality:

$$r(t_Q) = K_o + K_o \cdot \frac{h_{pf}}{z_f(s, t_Q) \cos \theta} \quad (58)$$

in which $z_f(s, t_Q)$ must be written in terms of the infiltration at time t_Q , or $G(s, t_Q)$, which in turn equals the cumulative rainfall at time t_Q (i.e., $G(s, t_Q) = R(t_Q)$). The formula expressing $z_f(s, t_Q)$ in terms of the cumulative rainfall $R(t_Q)$ is obtained by solving the quadratic Eq. (57) to yield the following result in this instance:

$$z_f(s, t_Q) = \frac{(n - a) - \sqrt{(n - a)^2 - 2eR(t_Q)\cos\theta}}{e} \quad (59)$$

where the following condition must be met for Eq. (59) to produce a real-valued answer when the coefficient e is positive:

$$\frac{(n - a)^2}{2e} \geq R(t_Q)\cos\theta \quad \text{if } e > 0 \quad (60)$$

Eq. (60) for $z_f(s, t_Q)$ must be substituted in Eq. (56), and, subsequently the time t_Q is that which achieves equality of the right-hand and left-hand sides of Eq. (58). The depth $z_f(s, t_Q)$ represents the initial boundary condition of the pde (56). The upstream boundary condition of Eq. (56) for time $t > t_Q$ is derived by setting the runoff depth to zero in Eq. (56) at $s = 0$ such that:

$$((n - a) - e \cdot z_f(0, t)) \cdot z_f(0, t) \frac{\partial z_f(0, t)}{\partial t} = -(K_o \cos \theta) \cdot z_f(0, t) + K_o \cdot h_{pf} \quad (61)$$

The upstream boundary condition for infiltration is derived from Eq. (57) once the depth to the wetting front at that location ($z_f(0, t)$) is solved for numerically:

$$G(0, t) = \frac{1}{\cos \theta} \left[(n - a) \cdot z_f(0, t) - \frac{e}{2} [z_f(0, t)]^2 \right] \quad (62)$$

The set of equations derived in this section, plus those presented governing runoff, can be solved to quantify infiltration, runoff, and translational slope stability when the antecedent water content varies linearly with increasing depth.

4.2. Continuity of suspended sediment and slope degradation: the role of infiltration

Water moving on the surface of the earth is a key agent of landform change. The processes of erosion, sediment transport, and sedimentation (or deposition) control how the land surface undergoes aggradation (rise of its elevation) or degradation (lowering of its elevation). The factors and processes governing erosion, sediment transport, and sedimentation by moving water are complex (Renard et al., 1997; Julien, 2010). This paper has shown infiltration influences slope runoff (and vice versa). This section develops the advective pde of 1D suspended sediment continuity involving slope degradation driven by runoff and infiltration. Fig. 16 depicts the variables and geometry that control the continuity (or conservation) of suspended sediment and slope degradation. Fig. 16 displays the (vertically-averaged) concentration of suspended sediment ($C_{ss}(s, t)$) and the thickness of slope degradation ($z_{sd}(s, t)$). The concentration of suspended sediment is herein defined as the volume of sediment (detached from the slope surface) per unit volume of water in the water column of depth d as shown in Fig. 16. The suspended sediment discharge (q_{ss}) advected by runoff equals the runoff rate multiplied by the sediment concentration, or $q_{ss} = qC_{ss}$ (it has units of volume of suspended sediment per unit time).

Slope degradation results from the detachment of sediment (or soil) from the slope surface that undergoes two types of downslope transport processes. One process produces the motion of detached sediment that remains in contact with the eroding surface as it rolls and slides downslope. The volume of sediment transported in this manner is called the "bed load". The bed load does not contribute to suspended sediment in the water column. The second process transports detached sediment in suspension. The volume of sediment transported in this manner is called the "suspended load". Sediment detachment occurs when the shear stress on the slope surface exerted by moving water exceeds the critical shear stress necessary to mobilize soil particles.

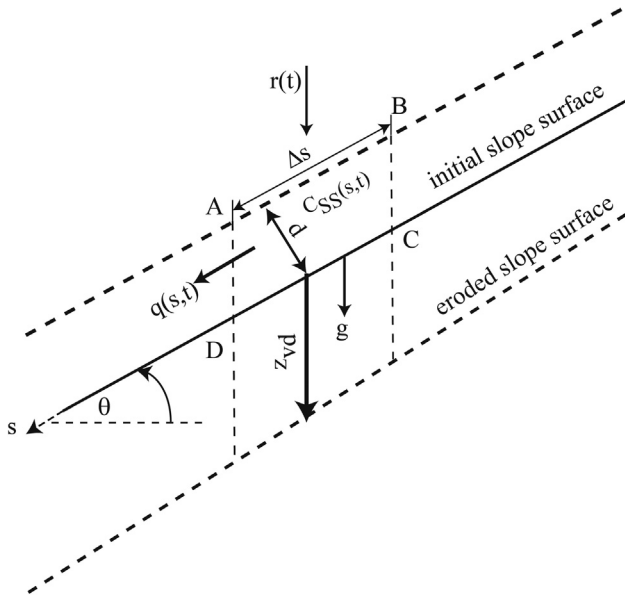


Fig. 16. Variables and geometry that control slope erosion. Elevation view not drawn to scale.

The transport of detached sediment particles depends on the specific runoff and particle characteristics. The critical shear stress of cohesive soils is commonly too large to be exceeded by the tractive shear exerted by shallow slope runoff (Smerdon and Beasley, 1961; Moody and Smith, 2005; Shan et al., 2015). The impact of raindrops, however, can exert stresses that break up the bonds between cohesive-soil particles prior to the initiation of runoff. Those particles may be transported by runoff thereafter as either bed load or suspended load depending on runoff and particle characteristics.

Let z_{vb} and z_{vs} denote respectively the thicknesses of slope degradation caused by bed-load and suspended-load transport. The corresponding volume of transported sediment are denoted respectively by V_{vb} and V_{vs} . The total slope degradation is the sum of the degradations caused by bed-load and suspended-load transport, $z_{vd} = z_{vb} + z_{vs}$, with a corresponding volume of transported sediment denoted by V_{vd} . The time-rate of change of the total volume of sediment transport equals the sum of the time-rate of change of the volume of sediment that is transported as bed load plus the time-rate of change of the volume of sediment transported as suspended load expressed by the following formula:

$$\frac{\partial V_{vd}}{\partial t} = \frac{\partial V_{vb}}{\partial t} + \frac{\partial V_{vs}}{\partial t} = \left(\frac{\partial z_{vb}}{\partial t} + \frac{\partial z_{vs}}{\partial t} \right) \cos \theta \cdot \Delta s \cdot b \cdot (1-n) \quad (63)$$

in which n denotes the porosity of the slope soil. The equation of continuity of suspended load (or suspended sediment) developed in this section considers (i) the sediment load advected with runoff, (ii) the sediment load carried onto the slope surface by infiltration, and (iii) the volume of sediment eroded from the slope surface that becomes suspended load in the overlying water column (V_{vs}). The balance of the rates of sediment in and out of the fluid control volume ABCD shown in Fig. 16 determines the rate of change of the concentration of suspended load in the control volume. The control body of water ABCD encompasses a volume equal to $b d \Delta s$, in which Δs denotes its dimension along the coordinate axis s . The pde describing the continuity of suspended sediment is given by the following expression:

$$-\frac{1}{b} \frac{\partial (q C_{SS})}{\partial s} - C_{SS} \cos \theta \frac{\partial G}{\partial t} + \cos \theta \cdot (1-n_F) \frac{\partial z_{vs}}{\partial t} = \frac{\partial (C_{SS} d)}{\partial t} \quad (64)$$

where n_F represents the porosity of the sediment fraction that becomes suspended. The initial condition associated with Eq. (64) prescribes zero sediment concentration at time t_Q when slope runoff begins. The

upstream boundary condition of Eq. (64) specifies the sediment concentration at $s = 0$ is equal to zero for all time following the initiation of runoff. The runoff depth (d , see the pde (19)) and the infiltration rate (see the pde (8)) are coupled with the sediment concentration (C_{SS}) governed by the pde (64). This constitutes a set of three coupled nonlinear pdes. The rate of slope degradation by suspension and transport of detached sediment ($\partial z_{vs}/\partial t$) must be specified to solve the runoff, infiltration, and sediment continuity equations. That rate must be expressed as a function of the runoff regime and sediment characteristics, including its resistance to shear detachment (see, e.g., Simons et al., 1981; Schiettecatte et al., 2008). In general, the rate of slope degradation introduces a fourth equation that must be coupled with the pdes for sediment transport, runoff, and infiltration to yield a tetrad of nonlinear equations. Their solution remains an unresolved research problem.

The rate of slope degradation can be solved for from Eq. (64) if steady-state conditions are approached (see Figs. 8 and 9). Setting the runoff rate equal to its steady-state value ($q(s,t) \rightarrow q(s)$) in Eq. (64) and assuming the suspended sediment concentration converges to a steady-state condition after sustained external constant wetting we have the following result:

$$\frac{\partial z_{vs}}{\partial t} = \frac{1}{b \cdot \cos \theta \cdot (1-n_F)} \frac{\partial [q(s) \cdot C_{SS}(s)]}{\partial s} + \frac{C_{SS}(s)}{(1-n_F)} g \quad (65)$$

Eq. (65) states the rate of slope degradation is proportional to the sum of the change of suspended sediment with respect to slope location plus the deposition of suspended sediment induced by infiltration.

5. Conclusions

This paper presented a theory for the calculation of slope runoff and infiltration, and for the assessment of translational slope stability based on a generalization of the G&A model to the case of sloping terrain. Several examples involving external water application (by rainfall) with different temporal distributions, and relying on soil and hydraulic characteristics, demonstrated the solution capacity of this paper's solution algorithm. The solution algorithm was found numerically stable and accurate, and its execution for several runs involving constant, triangular, or NRCS rainfall patterns required processing times of less than 10 min each in a standard laptop computer. This paper's results demonstrated long and sustained water application produces larger infiltration than triangular or NRCS-type rainfall distributions of the same duration and the same total depth of precipitation. Evidently, infiltration is more effective when the water application rate is constant, all other factors being equal. Therefore, the constant rainfall or water application poses a greater hazard to slope stability than the other rainfall types or water applications.

This paper introduced a novel interpretation of and solution method for the long-slope stability problem. It was shown by quantitative analysis that cohesionless and unsaturated soils forming sloping terrain are prone to translational sliding as the wetting front descends through the soil profile. This work demonstrated the stability of long slopes formed by cohesionless soils depends on basic factors, such as slope geometry, the water application rate, the depth of penetration of the wetting front, and the soil hydraulic and strength characteristics. There is no requirement in this paper's slope stability theory for discontinuities of hydraulic conductivity within the wetted soil profile or the formation of a perched groundwater flow system to explain slope stability. It was demonstrated, however, that compressed air or reduction of the hydraulic conductivity at any depth imposes a limiting slope angle to preserve stability. On the other hand, this paper has shown long slopes formed by cohesive soils are not likely to undergo shallow sliding by a penetrating wetting front.

The pde relating the continuity of suspended sediment to the rate of slope degradation caused by slope runoff and influenced by infiltration was developed in this work. The pde governing suspended sediment

concentration must be coupled with the pdes governing infiltration and runoff to form a system of three nonlinear pdes from which to calculate sediment concentration, runoff, and infiltration, provided the rate of slope degradation is unknown or is formulated in terms of runoff and soil resistance characteristics. The joint solution of the runoff, infiltration, sediment transport, and slope degradation equations for sloping terrain remains an unresolved research problem.

6. Symbology

The symbols L^* and t^* denote units of length and time, respectively; kN and kPa denote kilo Newtons and kilo Pascals, respectively.

a : antecedent volumetric water content at the slope surface depicted in Fig. 15 (dimensionless);

a_0 : coefficient defined in Eq. (9) ($L^* t^{*-1}$);

a_1 : coefficient defined in Eq. (10) ($L^{*2} t^{*-1}$);

$a_{k,k-1}^{(j-1)}$: recursive equation defined in Eq. (40) (dimensionless);

b : slope width (L^*);

b_0 : coefficient in the polynomial of Eq. (16) ($L^{*2} t^{*-4}$);

b_1 : coefficient in the polynomial of Eq. (16) ($L^{*2} t^{*-3}$);

b_2 : coefficient in the polynomial of Eq. (16) ($L^* t^{*-2}$);

$b_{k,k-1}^{(j-1)}$: recursive coefficient defined in Eq. (42) (L^*);

c : slope of the rising limb of triangular rainfall depicted in Fig. 3 ($L^* t^{*-2}$);

c' : effective cohesion of the slope soil (kPa);

C_{SS} : suspended sediment concentration (L^{*3} sediment L^{*-3} water);

d : runoff depth (L^*);

$d_0^{(j)}$: runoff depth at node $k = 0$ and time $j\Delta t$ (L^*);

$d_k^{(j_0)}$: runoff depth at node $k = 0$ and time $j_Q \Delta t$ when runoff begins (L^*);

$d_k^{(j)}$: runoff depth at node k and time $j\Delta t$ (L^*);

$d_k^{(j-1)}$: runoff depth at node k and time $(j-1)\Delta t$ (L^*);

$d_{k-1}^{(j-1)}$: runoff depth at node $k-1$ at time $(j-1)\Delta t$ (L^*);

d^* : average depth of runoff (L^*);

D_R : duration of rainfall (t^*);

D_S : specific water capacity (L^{*-1});

e_0 : slope of the antecedent volumetric water content deficit with depth shown in Fig. 15 (L^{*-1});

$f(s,z)$: equation describing the geometry of a boundary condition;

$f_{k,k-1}^{(j-1)}$: recursive coefficient defined in Eq. (44) (L^*);

FS : factor of safety (dimensionless);

FS_0 : factor of safety prior to slope wetting (antecedent factor of safety) (dimensionless);

g : infiltration rate ($L^* t^{*-1}$);

g^* : the acceleration of gravity ($L^* t^{*-2}$);

G : infiltration or infiltration depth (L^*);

G_t : derivative of infiltration with respect to time; it equals the infiltration rate ($L^* t^{*-1}$);

$G_0^{(j)}$: the infiltration at node $k = 0$ and time $j\Delta t$ (L^*);

$G_k^{(j)}$: infiltration at node k and time $j\Delta t$ (L^*);

$G_k^{(j_0)}$: the infiltration at node k and time $j_Q \Delta t$ when runoff begins (L^*);

$G_k^{(j-1)}$: infiltration at node k and time $(j-1)\Delta t$;

$G_{k-1}^{(j-1)}$: infiltration depth at node $k-1$ and time step $(j-1)\Delta t$ (L^*);

$G_{k,k-1}^{(j-1)}$: recursive coefficient defined in Eq. (41) ($L^* t^{*-1}$);

h : hydraulic head (L^*);

h_p : soil–water tension (positive), it is equal to the negative of the pressure head (L^*);

h_{pf} : soil–water tension at the wetting front (L^*);

h_{p0} : initial soil–water tension (at time = 0) (L^*);

$h_{k,k-1}^{(j-1)}$: recursive coefficient defined in Eq. (47) (dimensionless);

j : time index (= 1, 2, ..., T) (dimensionless);

j_Q : time index describing the initiation of runoff at time $j_Q \Delta t$ (dimensionless);

k : Index for computational node (= 1, 2, ..., M) (dimensionless);

K : unsaturated hydraulic conductivity ($L^* t^{*-1}$);

K_0 : saturated hydraulic conductivity ($L^* t^{*-1}$);

$n_F: K_{hp}$: the derivative of the unsaturated hydraulic conductivity with respect to the soil–water tension (t^{*-1});

L : slope length (L^*);

m : exponent in the kinematic-wave runoff equation (= 5/3);

n : porosity of the soil forming the slope (dimensionless);

n_F : porosity of the sediment fraction that is detached to become suspended load (dimensionless);

N : Manning's or hydraulic roughness coefficient of the slope surface (seconds \cdot meter $^{-1/3}$ to produce velocity in meters s^{-1});

r : rainfall rate ($L^* t^{*-1}$);

r_0 : constant rainfall rate ($L^* t^{*-1}$);

r_d : discrete value of rain depth occurring over a computational time step Δt (L^*);

$r_k^{(j)}$: rainfall depth falling on node k during time step Δt beginning at time $j\Delta t$ and ending at time $(j+1)\Delta t$ (L^*);

R : cumulative rainfall (L^*);

S_0 : slope of the terrain (change in vertical elevation per unit horizontal distance) (dimensionless);

q : runoff rate ($L^{*3} t^{*-1}$);

q_s : Darcian flux (specific discharge) along the coordinate s ($L^3 t^{*-1}$);

q_z : Darcian flux (specific discharge) along the coordinate z ($L^3 t^{*-1}$);

q_{SS} : suspended sediment discharge (L^{*3} sediment t^{*-1});

s : coordinate parallel to the slope surface increasing downslope (L^*);

t : time;

t_Q : time at which runoff begins;

v_0 : volumetric water content prior to rainfall (antecedent volumetric water content) (dimensionless);

v : volumetric water content (dimensionless);

V_{vb} : volume of soil eroded that becomes bed load (L^{*3});

V_{vd} : Volume of soil eroded that equals the volume of bed load plus the volume of suspended load (L^{*3});

V_{vs} : volume of soil eroded that becomes suspended load (L^{*3});

w_0 : antecedent volumetric water-content deficit (= $n-v_0$) (dimensionless);

$x_{k,k-1}^{(j-1)}$: recursive coefficient defined in Eq. (45) (L^*);

z : coordinate perpendicular to the slope surface increasing downwards from the surface (L^*);

z_v : vertical coordinate increasing downwards from a datum (L^*);

z_{vb} : thickness of soil eroded to become bed load (L^*);

z_{vd} : the thickness of soil eroded that becomes bed load plus the thickness of soil eroded that becomes suspended load (= $z_{vb} + z_{vs}$) (L^*);

z_{vf} : depth of the wetting front along the coordinate z_v (L^*);

z_{vs} : thickness of soil eroded that becomes suspended load (L^*);

β : hydraulic coefficient defined by Eq. (20) ($L^{*1/3} t^{*-1}$);

γ : unit weight of soil (or sediment) prior to external wetting (kN/L^{*3});

γ_0 : unit weight of saturated soil (or sediment) (kN/L^{*3});

γ_w : Unit weight of water (kN/L^{*3});

Δs : distance increment along the coordinate s ; also the inter-nodal distance or computational distance step (L^*);

Δt : computational time step;

θ : slope angle;

ϕ' : effective friction angle.

Acknowledgments

The computational software and facilities of the Department of Geography at the University of California, Santa Barbara, were instrumental to carry out the numerical simulations of this work. This research did not receive any specific grant from funding agencies in the public, commercial, or not-for-profit sectors. The authors declare there are no conflicts of interests pursuant to the contents of this paper.

Appendix A

The exact mathematical statement of the infiltration problem in sloping terrain

An Eulerian volumetric balance of water can be written for the REV of Fig. 2 that leads to the following 2D partial differential equation when the dimensions of the REV tend to zero:

$$\frac{\partial q_s}{\partial s} + \frac{\partial q_z}{\partial z} = -\frac{\partial v}{\partial t} \quad (\text{A1})$$

in which v denotes the volumetric water content. The following steps are taken to transform Eq. (A1) into a partial differential equation written in terms of the soil's properties obtained from its characteristic curves that express the water content and the hydraulic conductivity as functions of the soil water tension (see, e.g., van Genuchten, 1980; Lu et al., 2010): (i) substitute Eqs. (4) and (5) into Eq. (A1); (ii) introduce the rate of change of the hydraulic conductivity with respect to the soil water tension ($K_{h_p} = dK/dh_p$), (iii) introduce the time derivative of the volumetric water content with respect to the water tension in terms of the specific water capacity $D_s = -dv/dh_p$ (Hillel, 1982). Eq. (A1) is transformed into the following expression once steps (i), (ii), and (iii) are implemented:

$$\frac{\partial \left(K \frac{\partial h_p}{\partial s} \right)}{\partial s} + \frac{\partial \left(K \frac{\partial h_p}{\partial z} \right)}{\partial z} + K_{h_p} \sin \theta \frac{\partial h_p}{\partial s} + K_{h_p} \cos \theta \frac{\partial h_p}{\partial z} = D_s \frac{\partial h_p}{\partial t} \quad (\text{A2})$$

Eq. (A2) is the 2D partial differential equation describing the variation of the soil–water tension. It relies on a system of rotated coordinates aligned with axes parallel and perpendicular to the slope surface on the slope plane. Eq. (A2) reduces to the classic 2D Richards equation when the slope angle $\theta = 0$ and the coordinate axes are rotated clockwise 180° (see, e.g., Hillel, 1982, for a statement of the classic 2D Richards equation).

The initial condition associated with Eq. (A1) is given by:

$$h_p(s, z, t = 0) = h_{p0}(s, z) \quad (\text{A3})$$

in which $h_{p0}(s, z)$ expresses the initial distribution of soil–water tension within the domain of soil under study. The boundary condition on the slope surface ($z = 0$) is given by the following formula up to the time of runoff initiation:

$$q_z = r \cos \theta = K \cos \theta + K \frac{\partial h_p(s, 0, t)}{\partial z} \quad 0 \leq s \leq L; \quad 0 \leq t \leq t_Q \quad (\text{A4})$$

or by the following equation after runoff begins:

$$h_p(s, 0, t) = d \cos \theta \quad 0 \leq s \leq L; \quad t > t_Q \quad (\text{A5})$$

The time when runoff begins (t_Q) occurs when the component of rainfall along the z coordinate ($r \cos \theta$) exceeds for the first time the component of the infiltration rate expressed by the right-hand side of Eq. (A4). This time must be obtained by simulating the change in soil–water tension and the hydraulic gradient of pressure head on the surface ($z = 0$). Additionally, boundary conditions are necessary below the slope surface for full specification of the mathematical problem describing the variation of the soil–water tension within the slope soil caused by water application on the slope surface. One possible approach to achieve such specification is to define (by educated guessing) a geometric boundary described by a function $f(s, z)$ on which the soil–water tension is specified. Another possible approach is to define a boundary $f(s, z)$ describing the position of a phreatic surface on which the soil water tension equals zero, if such phreatic surface exists. The models Hydrus 1D and Hydrus 2D/3D simulate the movement of water, heat, and solutes in variably saturated media, and have several options for setting boundary conditions (see a review by Šimůnek et al., 2016). Evidently, realistic subsurface boundary conditions must be assumed for any solution of Eq. (A2) to be meaningful. Field data may be available to assist in the formulation of proper values for the subsurface boundary conditions. It is evident, thus, that a numerical solution of the mathematically exact formulation of the infiltration problem on sloping terrain with surficial water input requires specifying the subsurface boundary conditions and the determination of the time of initiation of runoff. These specifications introduce uncertainty not present when employing the modified G&A infiltration model introduced in this work.

References

- Bradford, S.F., Katopodes, N.D., 2001. Finite volume model for nonlevel basin irrigation. *J. Irrig. Drain. Eng.* 127, 216–223. [http://dx.doi.org/10.1061/\(ASCE\)0733-9437\(2001\)127:4\(216\)](http://dx.doi.org/10.1061/(ASCE)0733-9437(2001)127:4(216)).
- Brooks, R.H., Corey, A.T., 1964. Hydraulic Properties of Porous Media. Hydrology Paper 3. Colorado State University, Fort Collins, Colorado.
- Campbell, G.S., 1974. A simple method for determining unsaturated conductivity from moisture retention data. *Soil Sci.* 117, 311–314.
- Cedegren, H.R., 1989. Seepage, Drainage, and Flow Nets. John Wiley & Sons, New York.
- Chaudry, H.C., 1993. Open-Channel Hydraulics. Prentice Hall, Upper Saddle River, New Jersey.
- Chen, L., Young, M.H., 2006. Green Ampt infiltration model for sloping surfaces. *Water Resour. Res.* 42, W07420. <http://dx.doi.org/10.1029/2005WR004468>.
- Chow, V.T., 1959. Open-Channel Flow. McGraw-Hill Kogakusha Ltd., Tokyo.
- Courant, R., Friedrichs, K.O., Lewy, H., 1928. On the partial difference equations of mathematical physics. *Math. Ann.* 100, 32–74.
- Cunge, J.A., Holly Jr., F.M., Verwey, A., 1980. Practical Aspects of Computational River Hydraulics. Pitman Publishing Ltd., London.
- Dingman, S.L., 2015. Physical Hydrology. Waveland Press, Lone Grove, Illinois.
- Duncan, J.M., Wright, S.G., Brandon, T.L., 2014. Soil Strength and Slope Stability. John Wiley & Sons, Hoboken, New Jersey.
- Green, W.H., Ampt, G.A., 1911. Studies on soil physics, part I: the flow of air and water through soils. *J. Agric. Sci.* 4, 1–24.
- Griffiths, D.V., Marquez, R.M., 2007. Three-dimensional slope stability by elasto-plastic finite elements. *Géotechnique* 57 (6), 537–546.
- Hillel, D., 1982. Introduction to Soil Physics. Academic Press Inc., Orlando, Florida.
- Hydrologic Engineering Center, 2000. Hydrologic Modeling System HEC-HMS: Technical Reference Manual. United States Corps of Engineers, Davis, California.
- Iverson, R.M., 2000. Landslide triggering by rain infiltration. *Water Resour. Res.* 36 (7), 1897–1910.
- Johnson, J.M., Loáiciga, H.A., 2017. Coupled infiltration and kinematic-wave runoff simulation in slopes: implications for slope stability. *Water* 9, 327. <http://dx.doi.org/10.3390/w9050327>.
- Julien, P.Y., 2010. Erosion and Sedimentation, second ed. Cambridge University Press, Cambridge, UK.
- Lax, P.D., 1954. Weak solutions for nonlinear hyperbolic equations and their numerical computations. *Commun. Pure Appl. Math.* 7, 157–193.
- Lambe, T.W., Whitman, R.V., 1969. Soil Mechanics. John Wiley & Sons, New York.
- Loáiciga, H.A., 2005. Steady-state phreatic surfaces in sloping aquifers. *Water Resour. Res.* 41, W08402. <http://dx.doi.org/10.1029/2004WR003861>.
- Loáiciga, H.A., Huang, A., 2007. Ponding analysis with Green-and-Ampt infiltration. *J. Hydrol. Eng.* 12 (1), 109–112.
- Loáiciga, H.A., 2015. Groundwater and earthquakes: screening analyses for slope stability. *Eng. Geol.* 193, 276–287.

- Lu, N., Godt, J.W., Wu, D.T., 2010. A closed-form equation for effective stress in unsaturated soil. *Water Resour. Res.* 46, W05515. <http://dx.doi.org/10.1029/2009WR008646>.
- McDonald, M.G., Harbaugh, A.W., 1988. A modular three-dimensional finite-difference ground-water flow model: U.S. Geological Survey Techniques of Water-Resources Investigations, book 6, chap. A1, 586 p. Reston, Virginia, USA.
- Mein, R.G., Larson, C.L., 1973. Modeling infiltration during a steady rain. *Water Resour. Res.* 9, 384–394.
- Moody, J.A., Smith, J.D., 2005. Critical shear stress for erosion of cohesive soils subjected to temperatures typical of wildfires. *J. Geophys. Res.* 110, F01004. <http://dx.doi.org/10.1029/2004JF000141>.
- Morbidelli, R., Saltalippi, C., Flammini, A., Cifrodelli, M., Corradini, C., Govindaraju, R.S., 2015. Infiltration on sloping surfaces: laboratory experimental evidence and implications for infiltration modeling. *J. Hydrol.* 523, 79–85.
- Morbidelli, R., Saltalippi, C., Flammini, A., Cifrodelli, M., Picciafuoco, T., Corradini, C., Govindaraju, R.S., 2016. Laboratory investigation on the role of slope on infiltration over grassy soils. *J. Hydrol.* 543, 542–547.
- Morbidelli, R., Saltalippi, C., Flammini, A., Govindaraju, 2018. Role of slope on infiltration. *J. Hydrol.* 557, 878–886.
- Morel-Seytoux, H.J., 1980. Application of Infiltration Theory in Hydrologic Practice, HYDROWAR Program. CEP80-81HJM2. Engineering Research Center, Colorado State University, Fort Collins, CO.
- Rawls, W.J., Ahuja, L.R., Bakensiek, D.L., Shirmohammadi, A., 1992. Infiltration and soil water movement. In: Maidment, D.R. (Ed.), *Handbook of Hydrology* (Chapter 5). McGraw-Hill, New York.
- Rawls, W.J., Brakensiek, D.L., 1983. A procedure to predict Green and Ampt infiltration parameters. In: *Advances in Infiltration*. American Society of Agricultural Engineering, St. Joseph, MI, pp. 102–112.
- Renard, K.G., Foster, G.R., Weesies, G.A., McCool, D.K., Yoder, D.C., 1997. Predicting soil erosion by water: a guide to conservation planning with the Revised Universal Soil Loss Equation (RUSLE). United States Department of Agriculture (USDA) Agricultural Handbook No. 703. US Government Printing Office, Washington, D.C.
- Salvucci, G.D., Entekhabi, D., 1995. Ponded infiltration into soils bounded by a water table. *Water Resour. Res.* 31, 2751–2759.
- Schiettecatte, W., Verbist, K., Gabriels, D., 2008. Assessment of detachment and sediment transport capacity of runoff by field experiments on a silt loam soil. *Earth Surf. Processes Landforms* 33 (8), 1302–1314.
- Schuster, R.L., Salcedo, D.A., Valenzuela, L., 2002. Overview of catastrophic landslides of South America in the twentieth century. In: Evans, S.G., Degraff J.V. (Eds.), *Catastrophic landslides: Effects, Occurrence, and Mechanisms*. Reviews in Engineering Geology 15, 1–34, Geological Society of America.
- Shan, H., Shen, J., Kilgore, R., Kerenyi, K., 2010. Scour in Cohesive Soils. Publication No. FHWA-HRT-15-033, Federal Highway Administration, McLean, Virginia.
- Simons, D.B., Li, R.M., Fullerton, W., 1981. Theoretically derived sediment transport equations for Pima County, Arizona. In: Prepared for the Pima County Department of Transportation and Flood Control District, Tucson, Arizona. Simons, Li & Associates, Fort Collins, Colorado.
- Šimůnek, J., van Genuchten, M.Th., Šejna, M., 2016. Recent developments and applications of the HYDRUS Computer Software Packages. *Vadose Zone J.* <http://dx.doi.org/10.2136/vzj2016.04.0033>.
- Singh, V.P., 2017. Kinematic wave theory of overland flow. *Water Resour. Manage.* 31, 3147–3160 (10.1007/s11269-017-1654-1).
- Smerdon, E.T., Beasley, R.P., 1961. Critical cohesive forces in cohesive soils. *Agric. Eng.* 42, 26–29.
- Smith, G.D., 1984. *Numerical Solutions of Partial Differential Equations*. Clarendon Press, Oxford, UK.
- Strelkoff, T.S., Clemmens, A.J., 1994. Dimensional analysis in surface irrigation. *Irrig. Sci.* 15, 58–82.
- van Genuchten, M.T., 1980. A closed-form equation for predicting the hydraulic conductivity of unsaturated soils. *Soils Sci. Soc. Am. J.* 44, 892–898.
- Weill, S., Mouche, E., Patin, J., 2009. A generalized Richards equation for surface/sub-surface flow modelling. *J. Hydrol.* 366, 9–20. <http://dx.doi.org/10.1016/j.jhydrol.2008.12.007>.
- Wöhling, Th., Singh, R., Schmitz, G.H., 2004. Physically based modeling of interacting surface–subsurface flow during furrow irrigation advance. *J. Irrig. Drain. Eng.* 130, 349–356. [http://dx.doi.org/10.1061/\(ASCE\)07339437\(2004\)130:5\(349\)](http://dx.doi.org/10.1061/(ASCE)07339437(2004)130:5(349)).
- Zerihun, D., Furman, A., Warrick, A.W., Sanchez, C.A., 2005. Coupled surface–subsurface solute transport model for irrigation borders and basins. I. Model development. *J. Irrig. Drain. Eng.* 131 (5).